ORIGINAL ARTICLE

Surface finishing of additively manufactured IN718 lattices by electrochemical machining

Matthew E. Lynch[1] · Kerisha Williams[1,2] · Mariana Cabrera[3] · Tommaso Beccuti[3]

Abstract
Metal additive manufacturing offers design freedom, but high surface roughness can limit key properties such as fatigue and pressure drop. Machining all over is a common strategy to mitigate surface roughness, which unfortunately becomes technically and economically prohibitive in the case of significant geometric complexity, e.g., an internal lattice structure. In this paper, a strategy for finishing the surfaces of lattices using the commercial electrochemical machining (ECM) process COOLPULSE is proposed and demonstrated. Inconel 718 lattice coupons and complementing cathode tooling were designed and manufactured via laser powder bed fusion (LPBF). The tooling featured prongs to reach into the core of the lattice coupon in order to establish proximity between cathode and lattice surface (workpiece) as well as ports to allow electrolyte circulation in and around the lattice coupon. Both features extended the electrochemically active region into the core of the workpiece. Inspection of the processed lattice specimens revealed that a significant amount of material was removed from internal surfaces with accompanying improvement in roughness. Depth profiling indicated that the improvement of lattice surface state extended well into the core of the specimen without diminishment, in contrast to an external-only blasting process.

Keywords Surface finishing · Lattice · Additive manufacturing · Electrochemical machining · Surface roughness

1 Introduction

Additive manufacturing (AM) provides significant flexibility to create parts and components with unique and complex shapes. This flexibility extends to free-form parts, for example, those that have been optimized through topology optimization [1]. It is also enabling of lightweight, stiff lattice structures [2–4] that are filled volumetrically with nodes connected by ligaments. Lattices and cellular structures have application in the medical industry [5, 6] as well as emerging potential in aerospace [7–9] and other industries [10, 11]. One niche in aerospace is parts with a fixed aero skin that require internal support [12]. Furthermore, lattices can provide attractive multifunctional capabilities [13, 14].

Though AM is a capable means of creating 3D parts with complex shapes, components built using metal additive manufacturing tend to have high roughness, particularly on overhanging/downskin surfaces [15, 16], which trend in severity with surface orientation angle [17, 18]. Among the reasons driving this phenomenon is that upskin surfaces tend to have an underlying fast thermal transport pathway through solid material (melted and solidified in prior layers) [15], whereas the downskin orientation has a less thermally conductive pathway through powder which can lead to locally higher temperatures, melting below the current layer, and larger surface undulations upon solidification [19].

This roughness can sometimes be advantageous, in particular for heat transfer in heat exchangers and heat sinks [20, 21] or for bone in-growth and fixation in medical implants [22, 23]. Unfortunately, roughness can also be disadvantageous, for example, high pressure loss in a heat exchanger [20] or cooling architecture [24] as well as via degradation of mechanical properties. The technical impediment to finishing

✉ Matthew E. Lynch
  lynchme@rtx.com

1 Raytheon Technologies Research Center, 411 Silver Lane, East Hartford, CT 06108, USA

2 Present address: School of Materials Science and Engineering, Georgia Tech, 771 Ferst Drive, J. Erskine Love Building, Atlanta, GA 30332-0245, USA

3 Extrude Hone GmbH, Bgm.-Merk-Str. 1, 87752 Holzgünz, Germany

complex surfaces, and especially to finishing internal surfaces including lattices, has been identified as a significant barrier to adoption of additive manufacturing in industry [25].

One of the most affected mechanical properties is high cycle fatigue (HCF), which is sensitive to surface defects, stress concentrations, subsurface porosity, and other surface imperfections [26]. As-built surfaces of additively manufactured parts carry a significant stress debit [26] compared with the bulk properties of the material. That is, if the as-built surface is left intact, a part must be designed to a lower service stress than would be expected from measured fatigue properties of the bulk material (which are often obtained by removing surface material using a low-stress grinding operation). This debit can be on the order of 33% [27] in order to achieve the same lifetime (number of cycles) as a part with bulk properties and could potentially negate advantages associated with additive manufacturing. Higher roughness, particularly larger maximum pit height Sv, correlates with fewer cycles to failure [28]. In general surface post-processing operations tend to reduce roughness and improve fatigue performance [29, 30].

The HCF performance of an additively manufactured lattice is a function of geometric factors combined with material factors, which results in several competing mechanisms limiting fatigue life, notably cyclic ratcheting [31, 32] and fatigue crack initiation/growth [32–34]. The dominant mechanism can shift depending on unit cell design [35] and condition of lattice ligaments. Surface defects do appear to be among the primary factors in additive lattice fatigue damage development [32–37]. Therefore, as part of a larger HCF mitigation strategy also including unit cell design [35] and microstructural control [33], lattice surface condition (e.g., presence of defects, roughness) should be improved in order to mitigate reduction in fatigue life compared with bulk properties.

To improve the material properties of the surface back toward the level of the bulk, machining to remove the rough and defective outer surface layer is generally taken to be an effective strategy for AM parts [38–40]. Unfortunately, lattices are not able to be machined due to their geometric complexity and inability to access most surfaces with a machine tool. A variety of surface finishing processes exist as an alternative to machining [29, 30, 41]. Mechanical processes such as vibratory, tumbling, and centrifugal barrel finishing use abrasion to remove material from primarily external surfaces [40, 42]. Shot peening imparts compressive residual stress to the surface [30]. Chemical etching processes likewise use surface attack to remove material [43]. Electropolishing [30] and electrochemical machining (ECM) [44] oxidize metal atoms in the outer layer of a metal additive part which causes them to be removed and the surface to be smoothed. Figure 1a shows the anodic metal dissolution process with a $NaNO_3$ electrolyte. Conventional ECM requires a close approach between cathode and the surface of a workpiece (100–600 μm) [44], which limits application in additive parts.

Lattices and internal surfaces present challenges to these alternative surface finishing processes. Blasting or shot peening from the outside has a limited penetration depth into the core of a lattice part, and the high energy impact has the potential to damage the lattice [45]. Other abrasive strategies have been proposed to address the challenges of internal surfaces including modified abrasive flow finishing, magnetic abrasive finishing, and fluidized bed machining [46, 47], but little progress or proof of concept has been reported for lattices. The geometric complexity of lattices serves as a barrier to the use of ECM with its small standoff gap [44]. Moreover, characteristic nonuniformity of electropolishing suggests issues with finishing the interior of a lattice [48]. Nevertheless, chemical etching and electrochemical polishing of lattices have been reported [48–52] with improvement in fatigue performance [53], but many require use of hazardous chemicals such as hydrofluoric acid [49–52]. In some cases, chemical etching actually increases roughness by causing micro-pitting but may concomitantly enhance fatigue life [54]. Limited penetration depth of chemical etching into the core of lattice specimen has been reported [45].

COOLPULSE (CP) [55] is a commercial surface finishing process based on the anodic metal dissolution principle inherent to ECM (Fig. 1a), where the workpiece part to be machined is the anode (positively charged pole) and the tool is the cathode (negatively charged pole). The workpiece, cathode tooling, and insulation are assembled in a sometimes intricate fashion (Fig. 1b) depending on the complexity of the surfaces to be finished. Both cathode and anode are connected to a controlled DC current supply (Fig. 1c) and separated by a gap, while a conductive electrolyte solution is flowed between them through the gap. As a result, the electrochemical reaction forces the workpiece to release metal ions into the electrolyte where they form hydroxides. The dissolution effect improves the surface of the part. Critically, the gap between cathode and anode is larger, on the order of 3–4 mm, compared with traditional ECM processes. The large standoff distance, in principle, simplifies the shape of a cathode to address all lattice surfaces. The layout of the system is provided for reference in Fig. 1d.

This paper is intended to report (1) a novel cathode tool design that makes use of the large gap and (2) a proof-of-concept demonstration of the use of CP using this tooling. Systematic studies of parameters are reserved for future work. The paper is laid out as follows. In Section 2, design and fabrication of a lattice structure and cathode tooling are described, and characterization methods are presented. Experimental results of CP lattice processing on surface condition and lattice geometry are described in Section 3. Outlook and needs for improvement are discussed in Section 4.
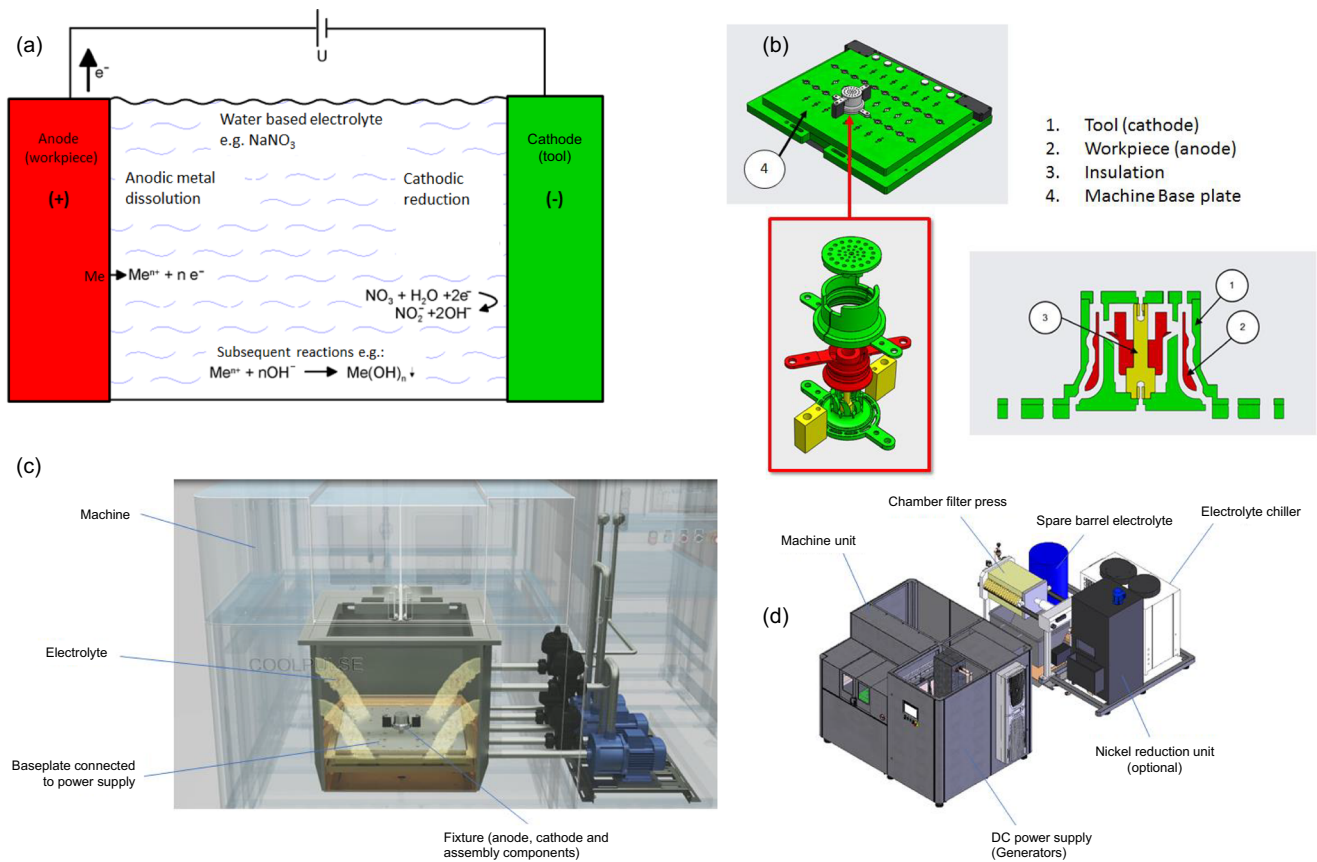
Fig. 1 **a** Principle of electrochemical machining (ECM) process with NaNO$_3$ electrolyte. General COOLPULSE setup: **b** tooling mode, **c** machine schematic diagram, and **d** system layout

2 Methods and materials

2.1 Specimen design and manufacturing

Small test coupons were designed with a lattice infill of 40% volumetric density (Fig. 2a and b). The side length of the coupons was 25 mm. The interior of the coupons was filled with cubic lattice unit cells having overall side dimension of 4 mm. Six ligaments intersected at each lattice node in a cubic pattern. Each lattice ligament had square cross section with 1.7 mm side length (Fig. 2c). Using square ligament cross sections as opposed to round provided flat surfaces that were easier to inspect than curved ligament surfaces. The lattice coupon also contained a cutaway for visual inspection of the interior. Though more advanced and exotic lattice designs are well-known, the lattice design used here was selected for the practical consideration of studying the suitability of the proposed process. The applicability to more advanced lattices should be studied in the future.

Lattice cubes were additively manufactured via laser powder bed fusion (LPBF) by C&A Tool Engineering, Inc. (Churubusco, IN, USA) on an EOS M280 using Inconel 718 powder. The specimens were oriented at 45° during the additive build to avoid flat ligament faces pointing directly

downward. Layer thickness was 40 μm. Following fabrication, the lattice specimens were stress relieved in a vacuum at 1066 °C and cut off the build plate. The exteriors were subjected to a low-intensity grit blast consisting of steel shot and size 8 glass bead (Fig. 2d)—referred to as the baseline condition in subsequent discussion—and processed by CP.

2.2 Tooling design and manufacturing

Based on the component's CAD model, a CP tool was designed to complement the coupon geometry for the purpose of improving the inner and outer surface of the specimen, as show in Fig. 3a. The driving principles were to (1) minimize the average gap between the cathode tooling and lattice surface and (2) flush the lattice interior with electrolyte to provide fresh reactant and remove reaction product. A simple consideration of Ohm's law in the electrolyte

$$U = IR = \frac{Js}{\sigma} \quad (1)$$

where U is the voltage drop, I is the current, and R is the resistance. Recognizing that I = JA where J is the current density and A is the area and also that R = s/(σA) where s is the

Fig. 2 Lattice specimen: **a**
exterior design, **b** vertical cross
section, **c** close-up cross
section, and **d** as-built baseline with light
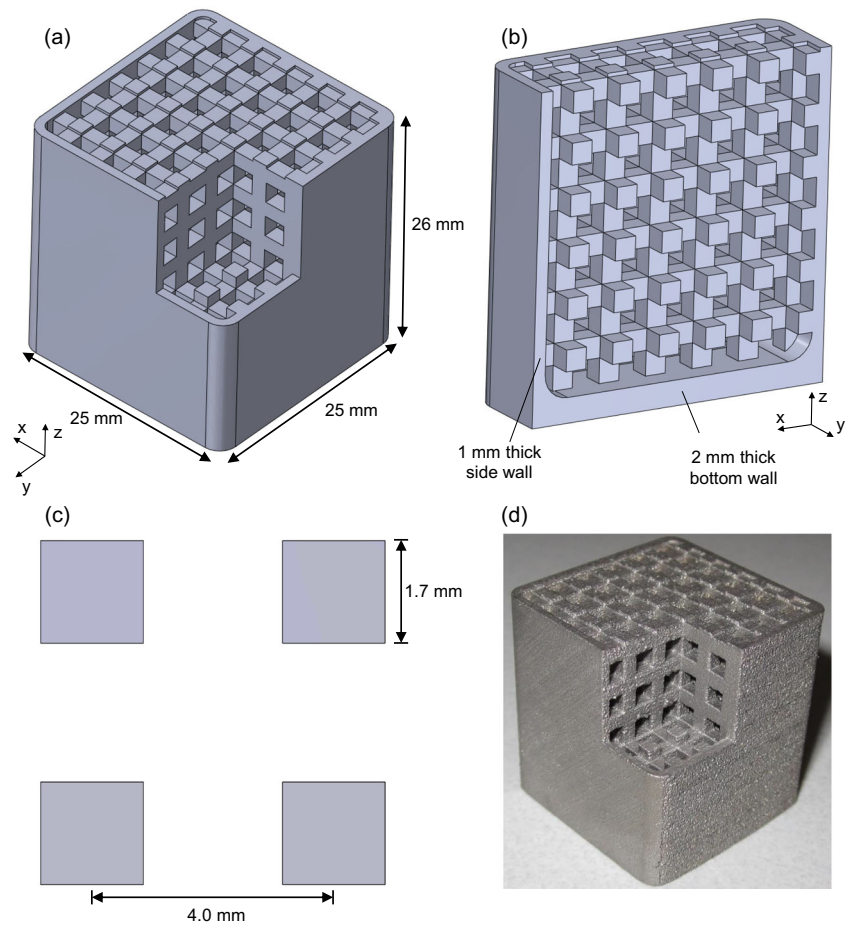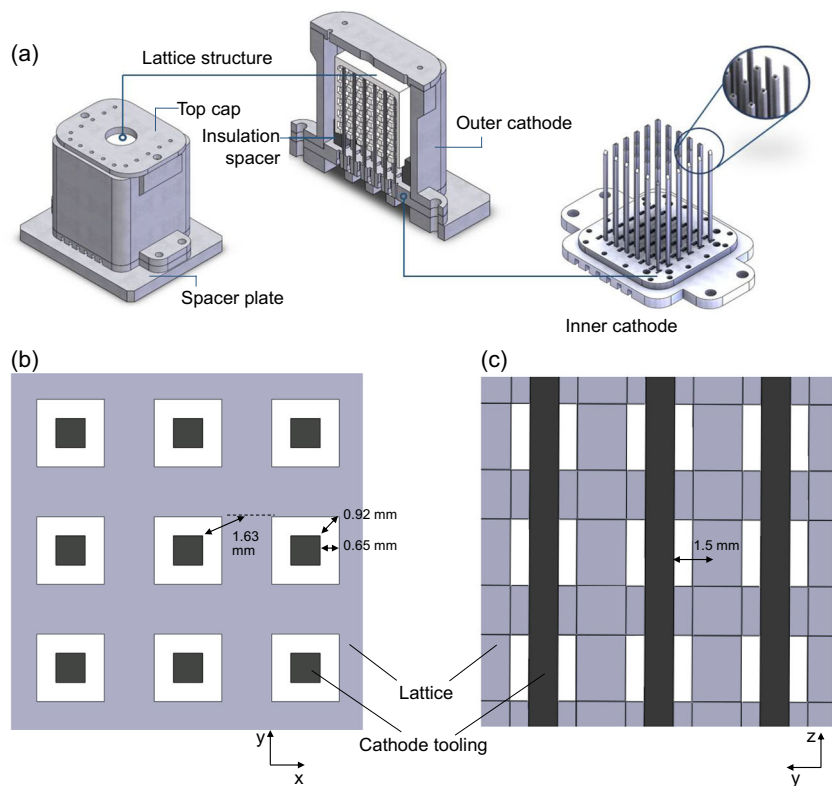grit blasting

(a)

26 mm

25 mm   25 mm

x z
y

(b)

1 mm thick
side wall

2 mm thick
bottom wall

z
x y

(c)

1.7 mm

4.0 mm

(d)

Fig. 3 **a** COOLPULSE tooling
(gray) for lattice structure (white)
and **b** cathode-workpiece separa-
tion distance analysis viewed
along inner cathode prong axis
and **c** viewed perpendicular to
cathode prong axis

(a)

Lattice structure

Top cap

Insulation
spacer

Outer cathode

Spacer plate

Inner cathode

(b)

1.63
mm

0.92 mm

0.65 mm

Lattice

Cathode tooling

y
x

(c)

1.5 mm

Lattice

z
y

gap between cathode and workpiece and σ is the conductivity, then the right hand side of Eq. (1) results. An inverse relationship between current density and gap is apparent, hence the imperative to minimize gap. When nonuniformity is present, total mass m removal can be expressed by an integral form of Faraday's law of electrolysis

$$m = \frac{M}{Fz} \int_{\Gamma} \int_{0}^{t} J(x,\tau)d\tau \mathrm{dx} \qquad (2)$$

where t indicates machining time, Γ indicates the surface of the lattice, x indicates position on the surface, M is the molar mass of the material being machined, F is Faraday's constant, and z is the valence number.

An outer cathode assembly was created to fit around the exterior of the cube. The tooling featured openings to allow for continuous flushing of electrolyte around the exterior and into the interior of the lattice specimen. An inner cathode with 29.5-mm-long prongs having 1.0×1.0 mm cross sections was created to address the interior lattice surface. The inner cathode was intended to be inserted into the lattice, with the prongs occupying the open space between ligaments. These prongs extended the reach of the cathode, reducing the gap between cathode and remote surface of the lattice and hence extending the region of electrochemical activity from the outside of the coupon into its core. Each prong featured a 0.5-mm-diameter cylindrical channel along its long axis which was intended to facilitate electrolyte flow to reach the lattice structure uniformly, flushing it to improve the effectiveness and homogeneity of the material removal process. The holes in the cathode plates also allowed the electrolyte to flow within the cathode, reaching the outer walls of the lattice structure. Care was taken to avoid contact between the lattice and the inner cathode in order to avoid a short circuit.

Co-design of both the lattice and the inner cathode was critical to use of CP. A straight insertion path for the inner cathode was provided by aligned lattice interstitials as depicted by the top-down view in Fig. 3b. Cathode prongs were designed based on the relatively large allowable cathode-workpiece gap characteristic of the CP process (3–4 mm) compared with the unit cell spacing. In the final design, distance from the exterior face of one cathode prong to immediately adjacent lattice face ranged from 0.65 to 0.92 mm (Fig. 3b). Distance to the centerline of adjacent lattice was 1.5 mm (Fig. 3c), and the maximum separation was 1.63 mm, occurring between the cathode prong and the middle of adjacent vertical lattice ligament skin as depicted in Fig. 3b. In all cases, interior lattice surface was closer than the 3–4 mm guideline for the maximum cathode-workpiece separation of CP. Separation between the exterior of the lattice coupon and outer cathode was around 4 mm.

Cathode tooling pieces (interior, exterior) were additively manufactured from Inconel 718, the same material as the lattice, via LBPF using an EOS M270 with 40-μm layer thickness by RTI Directed Manufacturing, Inc. (Pflugerville, TX, USA). The parts received a stress-relief heat treatment, were cut off from the build plate by wire electrical discharge machining (EDM), and subjected to a glass-bead grit blast. The individual pieces are shown in Fig. 4, including the inner cathode in Fig. 4a–b. The pieces were assembled with the aid of fasteners.

Given the high aspect ratio of the prongs, an expected risk of the inner cathode tooling design was deformation due to thermomechanical distortion from the AM build. Therefore, a fit-check was performed to ensure that the inner cathode tool could be inserted into the lattice coupon without physical contact. All full-size prongs were able to be inserted without issue. Unfortunately, there were a few prongs at the edges that did not pass the inspection. This was caused by the fact that the unit cells in these locations were truncated—that is, they were terminated prematurely by the wall and did not have the full 4-mm size. This caused the associated inner cathode prong to have unusually high aspect ratio and be more prone to distortion. In these few edge locations, the prongs were clipped off at the baseplate of the tool. This caused the immediately adjacent lattice to be left partially unfinished; fortunately this effect was confined to an edge of the specimen at the wall. The great majority of the specimen was able to be finished as planned. Future work should capture this effect in the lattice and/or tooling design stage.

The partially assembled tooling was installed into the CP equipment as shown in Fig. 5a. The lattice specimen was then placed over the inner cathode (Fig. 5b), protected from direct contact with the prongs by several insulating spacers (see Fig. 3). The top cap was then placed over the outer cathode and secured (Fig. 5c). Finally, contact between the lattice specimen and anode was made by fitting a contact tool through the central hole in the top cap, taking care to avoid direct contact with the top cap.

Process parameters listed in Table 1 were determined by CP software given the workpiece material (IN718) and desired material removal of 150 μm. A DC power supply (see Fig. 1d) creates the difference of potential needed between anode and cathode (7 V for this case). Based on the total surface to be processed, a current of 13 A per cycle was determined. A COOLPULSE 1000 system (able to provide 1000 A) was used for the work. In this system, concurrent processing of a batch of up to 76 lattice specimens is possible, subject to restrictions on the assembly size and layout (Fig. 1b–c). The standard electrolyte [56] was used, consisting of ethanediol, ammonium nitrate, ammonium chloride, ammonium sulphamide, and water. The electrolyte is flushed during the machining process to remove resultant metal hydroxide and filtered via the chamber filter press (Fig. 1d).

Fig. 4 Additively manufactured cathode tooling: **a**, **b** wide and close views of inner cathode, respectively, **c** outer cathode, **d** top cap, **e** spacer plate, and **f** cathode block bottom
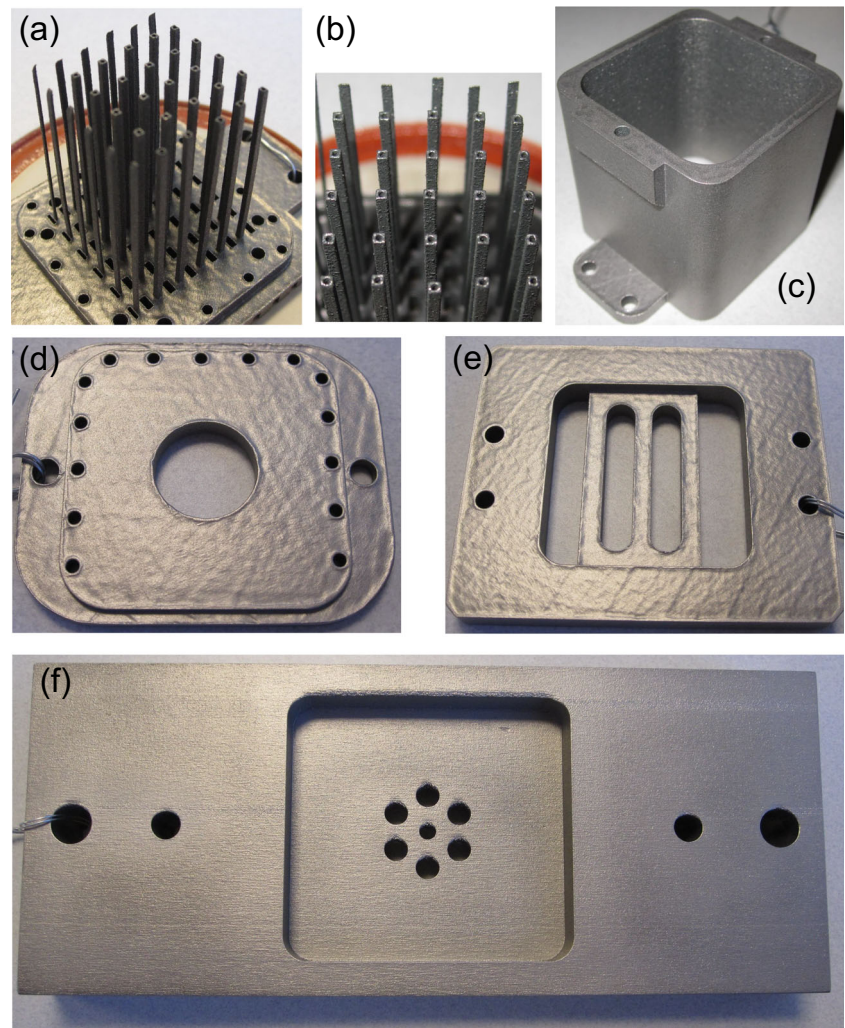
2.3 Inspection and analysis

White light interferometry (WLI) inspection of interior lattice surfaces was performed with a Zygo NewView 7300 with MetroPro v. 9.1.8 software removing 4th order waviness. Average roughness parameter Sa was computed, as defined in Eq. (3) [57] where A is the measurement area and $z(x,y)$ is the distance between the measured surface and mean plane.

Fig. 5 Cathode tool assembly and installation in COOLPULSE equipment: **a** before insertion of lattice specimen, **b** with lattice specimen, and **c** with top cap
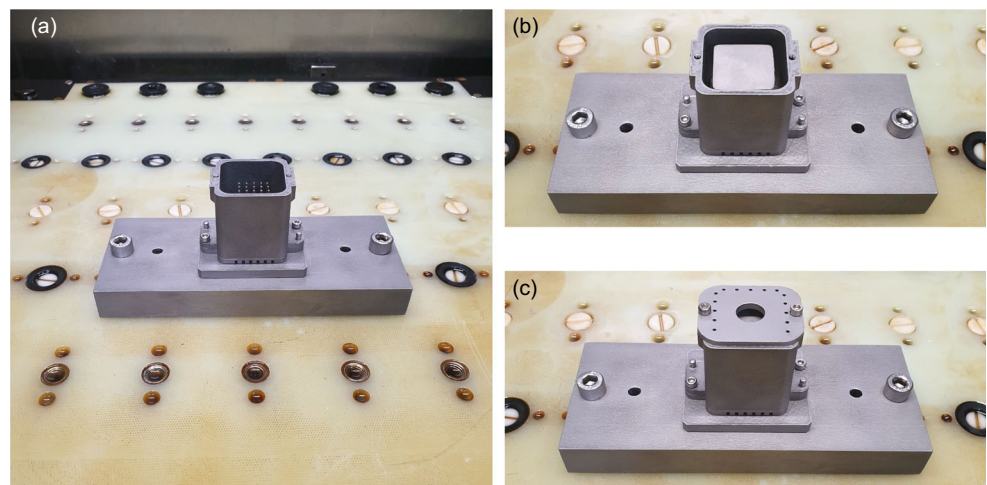
Table 1 COOLPULSE machining parameters

Parameter	Setting
Potential difference	7 V
Current	13 A
Electrolyte	COOLPULSE ES-G8020
Cycle time	30 min

$$S_a = \frac{1}{A} \iint\limits_A |z(x,y)| dxdy \tag{3}$$

In order to perform inspection of interior lattice ligaments, the coupons were sectioned along a plane as shown in Fig. 6a. The two resulting pieces were referred to as sides A and B. Due to the 45° build angle, side A surfaces exposed by the cut plane were downskin surfaces, whereas exposed side B surfaces were upskin. Horizontal and vertical ligament surfaces were examined, and the results were tracked according to the nomenclature indicated in Fig. 6b–c, where H indicates a horizontal ligament and V indicates a vertical ligament. The first number refers to the ligament row, and the second number indicates the ligament column. Thus, AH34 indicates a horizontal ligament in the third row from the top and fourth column from the left of side A.

In addition to WLI, specimens were examined by optical stereomicroscope (Olympus SZH10) and scanning electron microscope (SEM, Phenom XL desktop SEM). The specimens were cleaned in acetone prior to SEM to remove organic residue. Finally, lattice ligament thicknesses were measured using a digital caliper.

3 Results

Images of specimens before and after CP processing are given in Fig. 7. The exterior surface was notably more reflective after CP processing than the baseline condition. Lattice ligaments of the CP-processed specimen visible from the exterior were also noticeably thinner than those of the baseline specimen, reflecting significant material removal.

The CP-processed specimen did have unfinished regions caused by (1) high-aspect ratio prongs having been removed at the edge due to distortion or (2) surface covered by insulating contact. Both issues could be mitigated in the future depending on specimen and tooling design. Additionally, burn marks were present on the exterior associated with the electrode contact; to avoid burning, lattice coupons could be fabricated with sacrificial contact tabs.

High-resolution stereoscope views of the exterior of the top-most lattice unit cell show the effect of CP processing on exterior lattice surfaces. Baseline specimens (Fig. 8a) had a visually apparent rough surface. CP processing (Fig. 8b) caused ligaments to appear thinner due to removal of material. Significant rounding of corners also occurred due to material removal. In addition, the CP-processed surface became very reflective, indicating transformation of rough texture to smooth.

The average thickness of the top row of ligaments perpendicular to the section plane (normal to Fig. 6a section plane) was determined by measurement with a digital caliper (Table 2). The baseline lattice was 2.08 and 2.07 mm on sides A and B, respectively. Lattice subjected to CP processing was thinner on both sides, 1.63 and 1.64 mm, respectively, amounting to approximately a 22% reduction in thickness versus baseline.
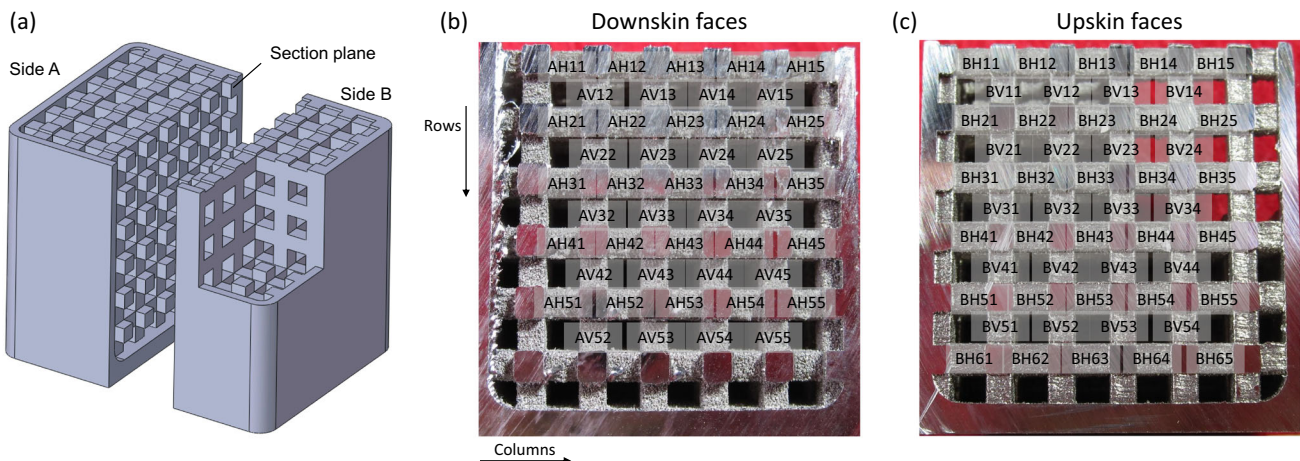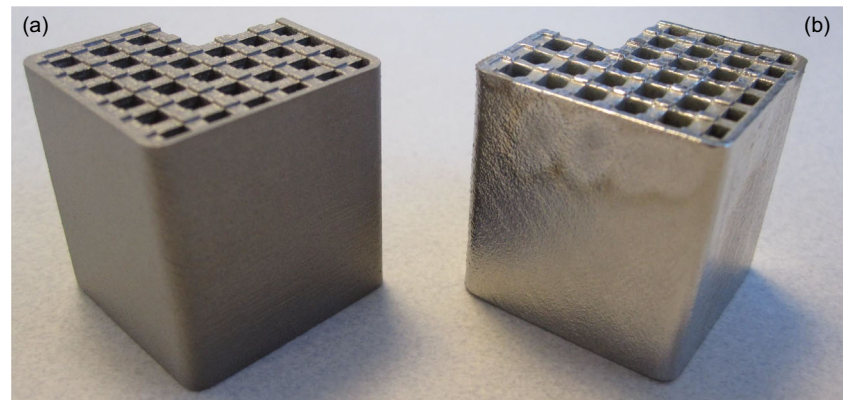

Fig. 6 **a** Specimen sectioning for internal inspection and **b** nomenclature for internal inspection locations on side A and **c** side B. H and V signify horizontal and vertical ligaments, respectively. First number is row, second number is column

Fig. 7 Lattice coupons **a** baseline
and **b** after COOLPULSE
processing

3.1 Downskin surfaces

An inspection of the interior surfaces of the coupon revealed similar improvement to the state of lattice surfaces. Pictures of cross sections under varying conditions are given in Fig. 9 for side A downskin surfaces. Visually rough texture were present on both vertical and horizontal ligaments in the baseline condition, as expected due to the lack of support leading to
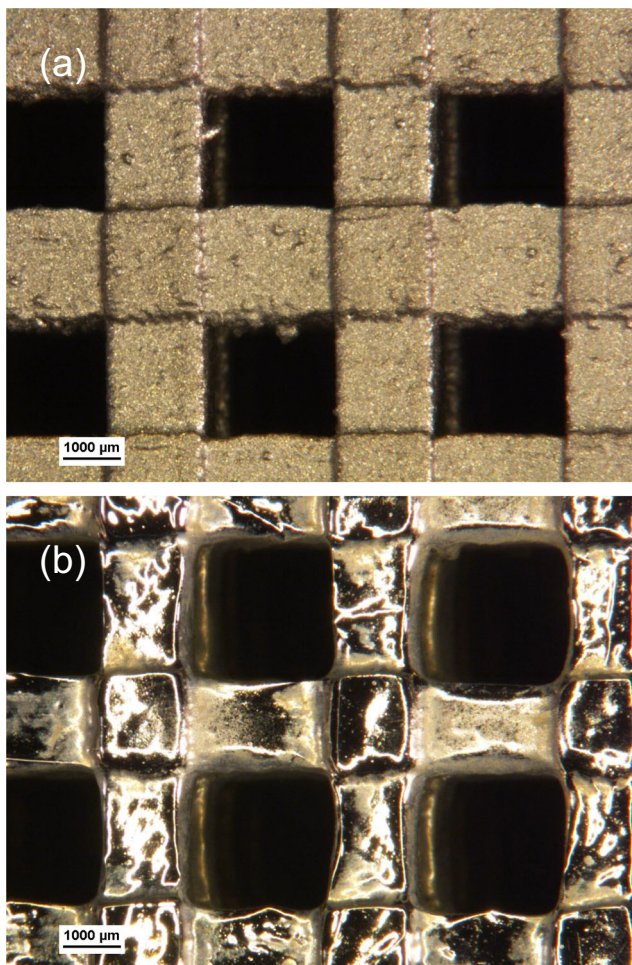

Fig. 8 Stereoscope images of exterior of **a** baseline and **b** after COOLPULSE processing

unsteadiness of the melt pool. The texture varied slightly in baseline condition (Fig. 9a) due to the light grit blasting of the exterior, especially from the upper left corner to the lower right corner. In contrast, CP processing transformed the surface in all regions of the cross section (Fig. 9b and d), changing it from matte to reflective with fine-scale features removed, though the surface did retain some coarse uneven texture.

In-plane thickness values measured by digital caliper are shown in Fig. 10 for both horizontal and vertical lattice ligaments. The figure plots mean thickness (average of all columns in a row) versus row where higher row number corresponds to deeper into specimen core (see Fig. 6b). The baseline condition displayed relatively constant thickness as a function of row. The CP-processed specimen showed ligament thickness reduction compared with the baseline: approximately 9% for horizontal ligaments and 6% for vertical ligaments versus baseline. These data are consistent with appreciable material removal over the volume of the lattice. The measured ligament thickness of CP horizontal specimens was lower at low row numbers (closer to exterior of specimen) and increased as row number increased (deeper into specimen core). This correlates to greater material removal at the mouth of specimen, decreasing with distance into the interior. It was suspected that this was caused by greater electrochemical reaction rate at the mouth brought on by more efficient flushing of the electrolyte; that is, more vigorous flow from outside the specimen reduced concentration polarization relative to the core. The difference between the thickness reductions

Table 2 Average out-of-plane thickness of horizontal ligaments in top row of side A and side B

Location	Baseline	With COOLPULSE
AH1	2.08	1.63
BH1	2.07	1.64

Out-of-plane refers to the direction normal to the section plane in Fig. 6a. Units are mm

Fig. 9 Internal views of downskin surfaces (side A) along section plane: **a**, **c** baseline lattice and **b**, **d** after COOLPULSE processing. Stereomicroscopy used for (**c**) and (**d**), in vicinity of location AV53 (near the bottom of the cavity)
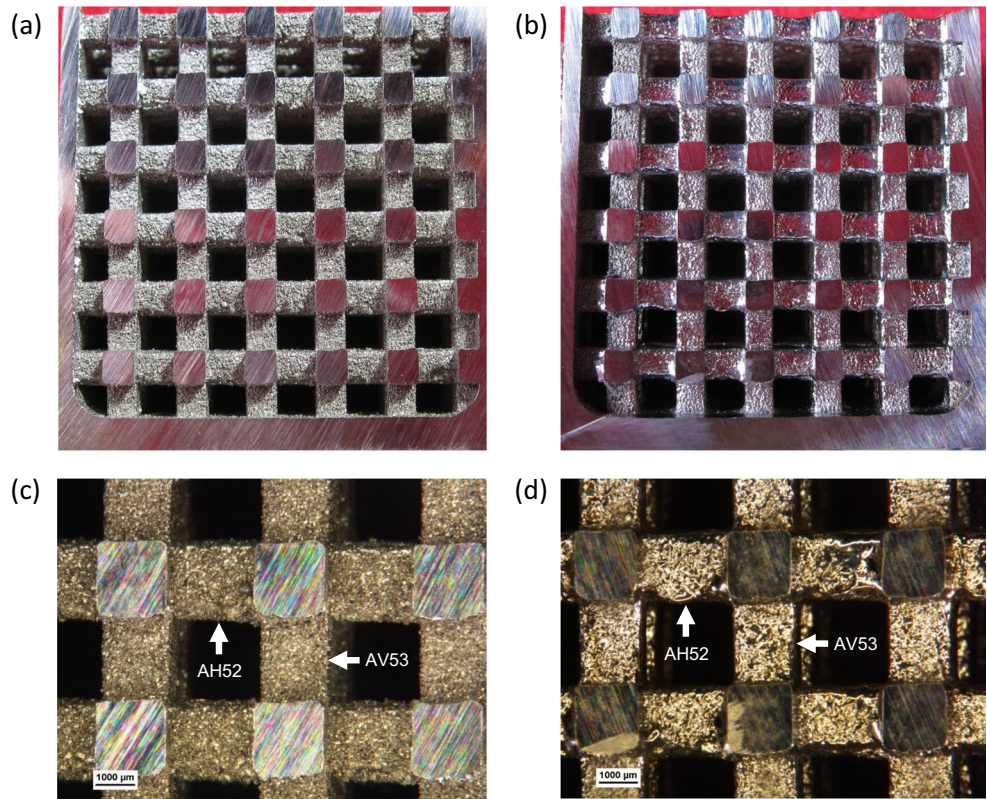

observed in horizontal versus vertical ligaments was attributed to higher electrochemical reaction rates caused by differences in ohmic polarization. Horizontal ligaments were separated by less distance (0.65 mm, see Fig. 3) from the cathode prongs compared with vertical ligaments (0.92 mm at closest approach), thus resulting in lower losses from charge transport in the electrolyte.

In the vicinity of location AV53, WLI indicated the elimination of fine-scale feature characteristic of the baseline surface in favor of larger-scale wavy features after CP processing (Fig. 11a–b). WLI scans of vertical ligaments from near-exterior (location AV13) to bottom of cavity (location AV53) further revealed a slight increase of Sa into the core of the lattice in the baseline condition (Fig. 11c). In contrast, roughness was uniformly reduced for the lattice subjected to CP, with an average of Sa = 10.9 μm. The trend of roughness is consistent with the trends of ligament thickness (i.e., material removal) in Fig. 10. Notably, the improvement of surface condition well into the core of the lattice specimen contrasts with the limited penetration depth reported for a chemical etching-only process [45] and external blasting.

Fig. 10 Average in-plane ligament thickness by row (top to bottom) in side A, see Fig. 6b for row position diagram
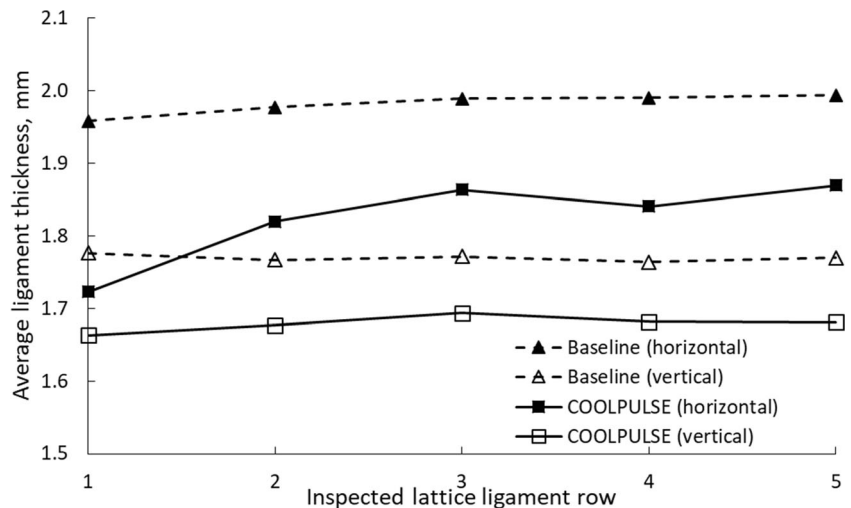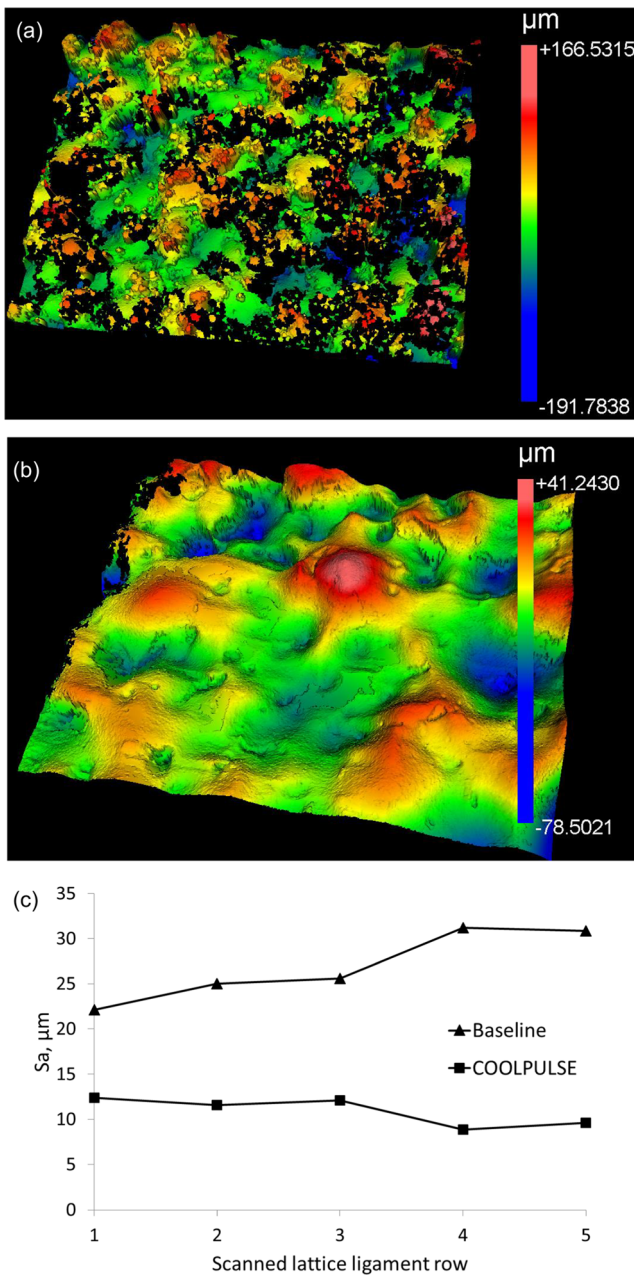
Fig. 11 WLI topography of lattice measured at internal scan location AV53: **a** baseline and **b** after COOLPULSE processing. **c** Depth profile of areal average roughness (Sa) of side A lattice interior as measured by WLI. Scan locations were along the third column of vertical ligaments, from location AV13 to AV53

Fig. 12 SEM investigation of side A **a** baseline and **b** COOLPULSE at horizontal ligament location AH52. See Fig. 6 for position diagram

SEM inspection provided a higher resolution view of the surface state before and after CP. Images from side A are given in Fig. 12 in the baseline (a) and CP-processed conditions (b) at location AH52. The baseline condition was characterized by a significant amount of partially melted powder. Below the adhered spheroids, large undulations in the surface are apparent leading to peaks and valleys seemingly penetrating far into the surface.
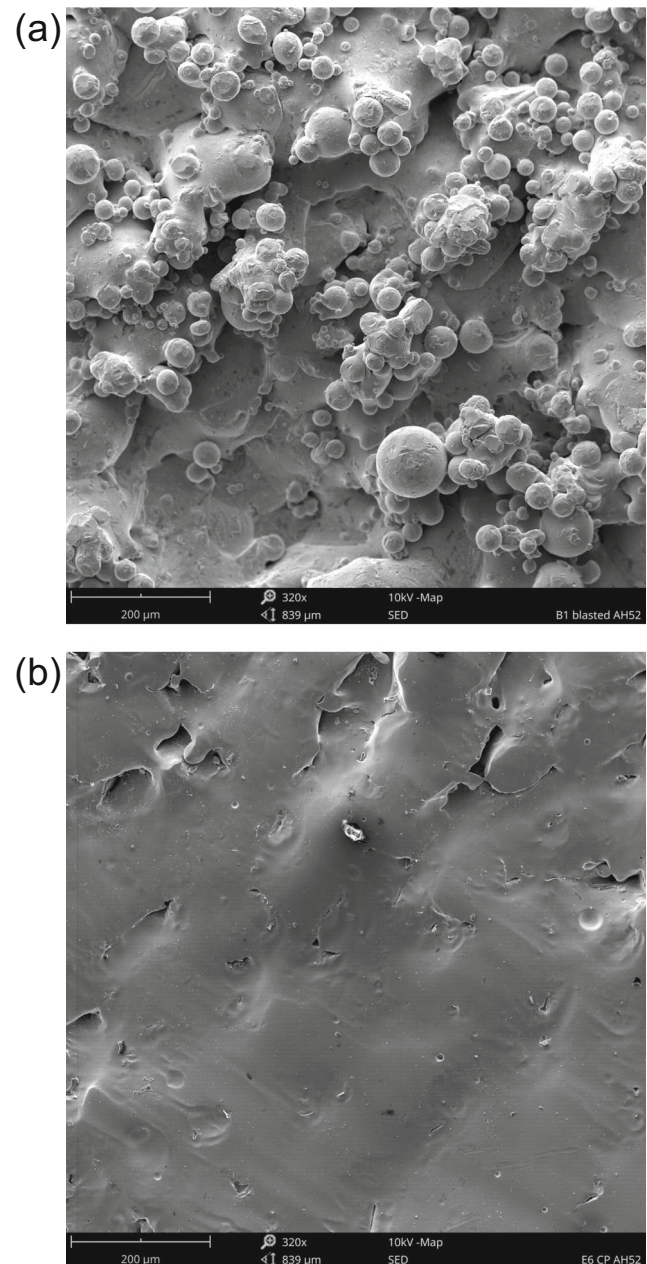
Specimens subjected to CP processing (Fig. 12b) did not have partially melted powder adhered to the surface. The surface also appeared significantly flattened and smoothed, consistent with preferential material removal at the peaks of the surface. This correlates to an optically bright appearance as seen in Fig. 9b and d. Some trenches were present, which were likely the remnants of the deepest valleys in the baseline condition. Given the general smoothing and flattening observed on the processed surfaces, longer duration of the CP process was expected to remove sufficient material depth that these valleys would also be eliminated.

Fig. 13 Internal views of upskin surfaces (side B) along section plane: **a**, **c** baseline lattice and **b**, **d** after COOLPULSE processing. Stereomicroscopy used for (**c**) and (**d**), in vicinity of internal scan location BH51 and BV51 (near the bottom of the cavity)
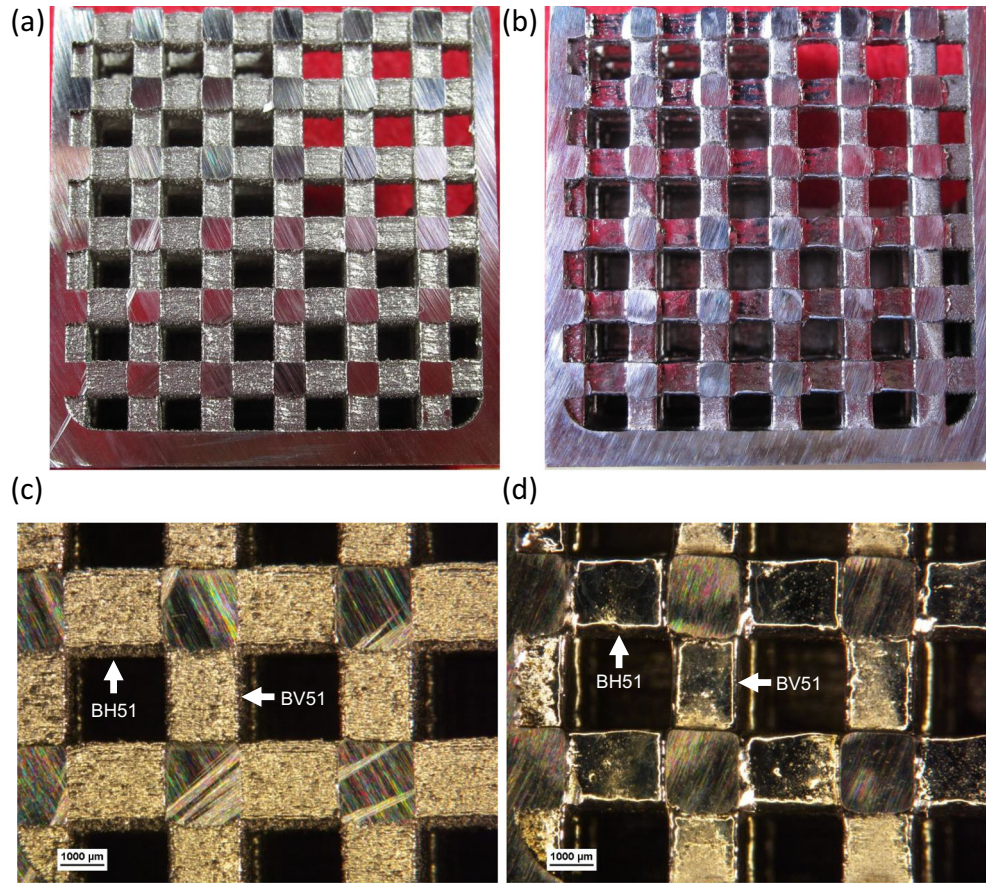

3.2 Upskin surfaces

The result for upskin surfaces (side B) are shown for CP processing (Fig. 13b) versus baseline condition (Fig. 13a). These surfaces were inherently less rough in the initial condition due to their upskin orientation, due in part [15] to fast thermal transport through solid material as opposed to slow transport through unmelted powder in the downskin orientation [19]. CP processing resulted in a smoother and brighter appearance. The horizontal ligaments of Fig. 13b appear to have been improved more than the vertical ligaments. This difference is suspected to be caused by the closer proximity of the horizontal ligaments to the cathode tool prongs (see Fig. 3), which therefore caused a higher degree of anodic dissolution of the lattice.

Fig. 14 Average in-plane ligament thickness by row (top to bottom) in side B, see Fig. 6c for row position diagram
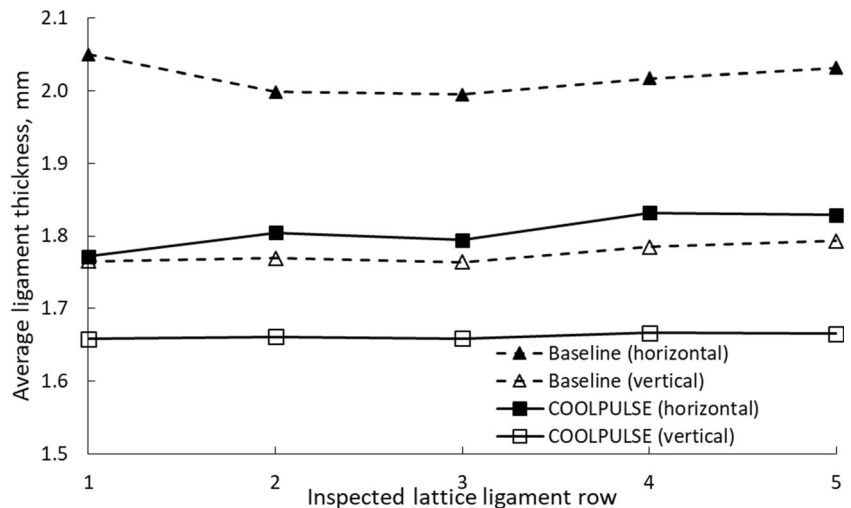
Optical stereomicrograph images in Fig. 13c and d show the baseline and CP-processed conditions, respectively. The horizontal ligament faces, e.g., BH51, were improved by CP to a mirror-like finish due to their proximity to the cathode tool. The vertical faces, e.g., BV51, were also significantly improved from the initial state. Being somewhat further from the cathode tool and not oriented normal to it, however, some regions of vertical ligament surfaces were not finished as uniformly as on the horizontal ligaments, particularly near the ligament junctions where electrolyte transport is relatively restricted. The vertical ligaments in row 6 (e.g., BV61, see Fig. 6) were not finished as well as those in row 5 because the tooling was not long enough to provide good proximity.

In-plane thickness values on side B measured by digital caliper are shown in Fig. 14 for both horizontal and vertical lattice ligaments. Again, CP processing was associated with a substantial reduction in thickness corresponding to material removal.

Both horizontal and vertical ligaments were inspected by WLI (Fig. 15) in the baseline (a) and CP-processed (b) state. Partially melted attached powder was apparent on the surface but to a lesser degree than observed on the downskin surface, attributed to the containment of the melt pool in this orientation which avoids partial melting of adjacent powder [19]. Similar changes in surface topography caused by CP processing were observed as in the previous examples along with the trend with depth (Fig. 15c). Sa was significantly lower in the CP-processed state than in the baseline state in every location measured: average Sa in lattice column 1 was 1.7 μm versus 6.8 μm for horizontal ligaments and 2.9 μm versus 6.1 μm for vertical ligaments.

SEM images of the upskin surfaces in Fig. 16 (location BH51) show that the topography of the surface in the baseline condition (a) is inherently less rough than observed in Fig. 12. There was partially melted powder present, but not to the degree seen on the downskin surface. Likewise, there are observable peaks and valleys, but their amplitudes are likewise much less than on the downskin. Starting from a state of less surface texture, the surface of the CP-processed specimen (Fig. 16b) was much flatter in the final condition, which was again consistent with optically bright surface as well as notable reduction in roughness observed by WLI. The very smooth state is an indication of how additional processing time could affect the downskin surface from Fig. 12b.

3.3 Effect of working distance

Separation of anode and cathode is a major factor in electrochemistry. The requirement for a small gap is a major limitation of traditional ECM, and, though CP allows larger separations, it was suspected to influence the results in this study. A graded surface state is visualized in Fig. 17, where the topography of a side B vertical ligament appears to vary depending on location. The right-most side of the SEM image is at the edge and shows where the ligament's surface turns the corner and becomes perpendicular to the plane of the image. The surface is the smoothest at this location. Moving from right to left, the surface becomes rougher until at the left-most side of the image distinct surface features are observable. This location corresponds roughly with the center of the ligament, and, if the field of view was moved to the left, the surface
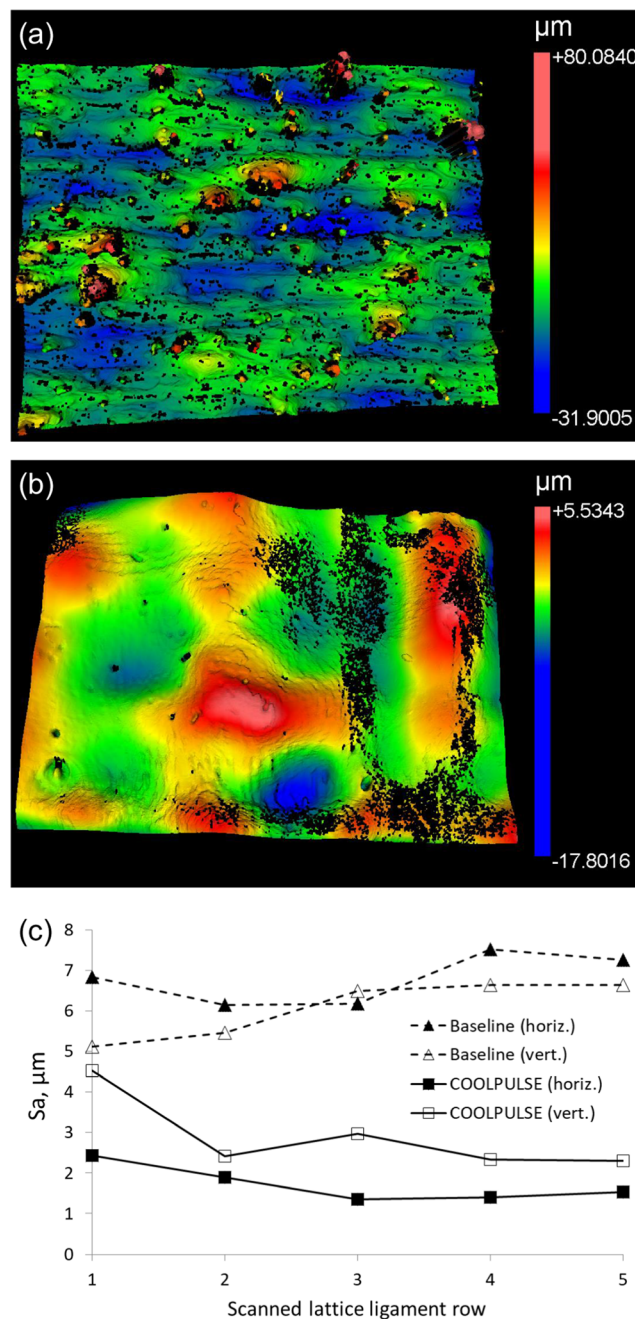

Fig. 15 WLI topography of upskin surfaces (side B) of **a** baseline and **b** COOLPULSE-processed specimens at location BH51. **c** Areal average roughness depth profile from side B, horizontal locations in column 1 (BH11-BH61) and vertical locations in column 1 (BV11-BV61). See Fig. 6c for row position diagram

Fig. 16 SEM investigation of upskin surfaces (side B) **a** baseline and **b** after COOLPULSE processing at horizontal ligament location BH51 (see Fig. 6c for position diagram)
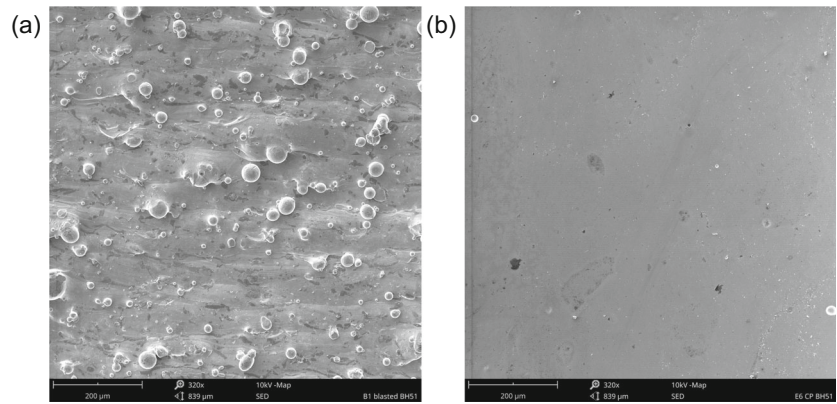
would become smoother as it approached the left edge of the ligament. The rough topography is likely due to the greater distance between the surface and the electrode in this location (see Fig. 3) at the edge, which results in less material removal due to greater ohmic polarization across the electrolyte. Managing this effect is expected to be important to future work.

The trend in roughness also varies in the vertical direction. The top of the image in Fig. 17 is just below the junction with another ligament. High roughness is apparent below this junction nearly to the edge of the ligament on the right side (note that the very rough surface in the upper left edge of the image is displaced material from sectioning the ligaments, not original surface roughness). It was suspected that this effect was caused by greater concentration polarization due to the cross-ligament blocking circulation of electrolyte.
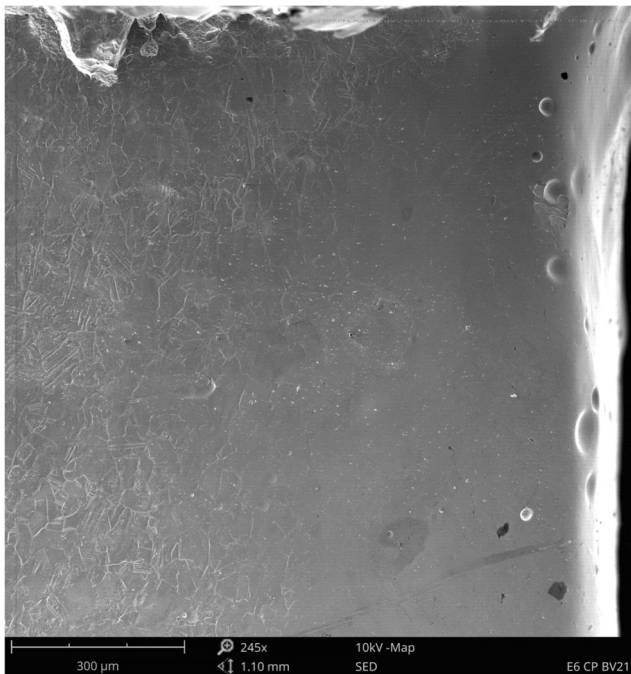

Fig. 17 SEM image of vertical ligament of COOLPULSE-finished specimen, side B (location BV21), with gradient in surface state

3.4 Comparison to external blasting

Additional as-built (without any grit blasting or CP processing) specimens were subjected to a high-intensity external blast consisting of compressed air, organics, and solid media. The blasting process was applied in a manner intended to reach as far into the core of the cavity as possible in order to thoroughly finish the internal lattice surfaces. This external blast process resulted in a pronounced gradient in appearance of internal surfaces along the cut section (Fig. 18a). Lattice surfaces closer to the outside appeared bright (upper left), but those more than a few unit cells' distance away from the external surface (lower right) appeared unaffected. Stereomicroscope inspection showed that internal surfaces far from the exterior (Fig. 18b) retained their very rough texture, while those located on the outside (Fig. 18c) were significantly affected. The trend contrasts with that observed for CP in the preceding sections, where the CP-based process results in relatively more uniform material removal throughout the core of the lattice.

Similarly, lattice ligament thickness varied strongly from the exterior to interior (Fig. 19a), again contrasting with the trend observed for CP. The high-intensity external blast condition resulted in low thickness in row 1 that increased rapidly as a function of row, increasing nearly to the level of unfinished condition by row 3. This trend is consistent with the lack of penetration of the exterior-only process into the core. The CP-processed condition displayed relatively uniform thickness. Measured surface roughness also showed a similar trend (Fig. 19b).

4 Discussion

The results shown here demonstrate the possibility of removing significant material from very rough as-built surfaces far into the core of a lattice. SEM inspection showed that the amount of material varied as a function of relative position on the lattice. Surface improvement was observed in all
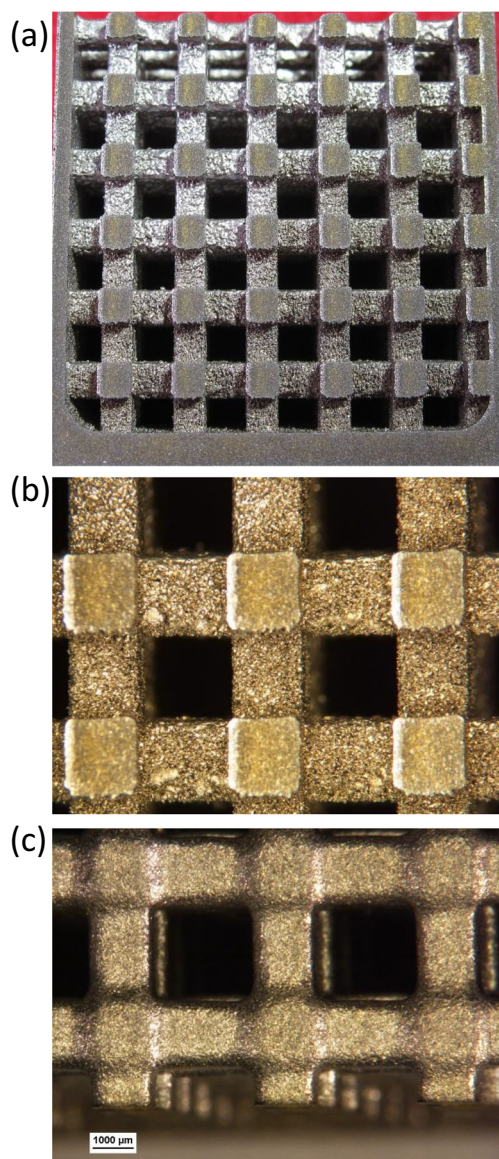
Fig. 18 Sectioned specimen subjected to high-intensity external blasting (side A). **a** Photo of entire interior cross section showing downskin surfaces, **b** stereomicroscope image of interior downskin surfaces in vicinity of location AV53, and **c** stereomicroscope image of exterior (top) surfaces
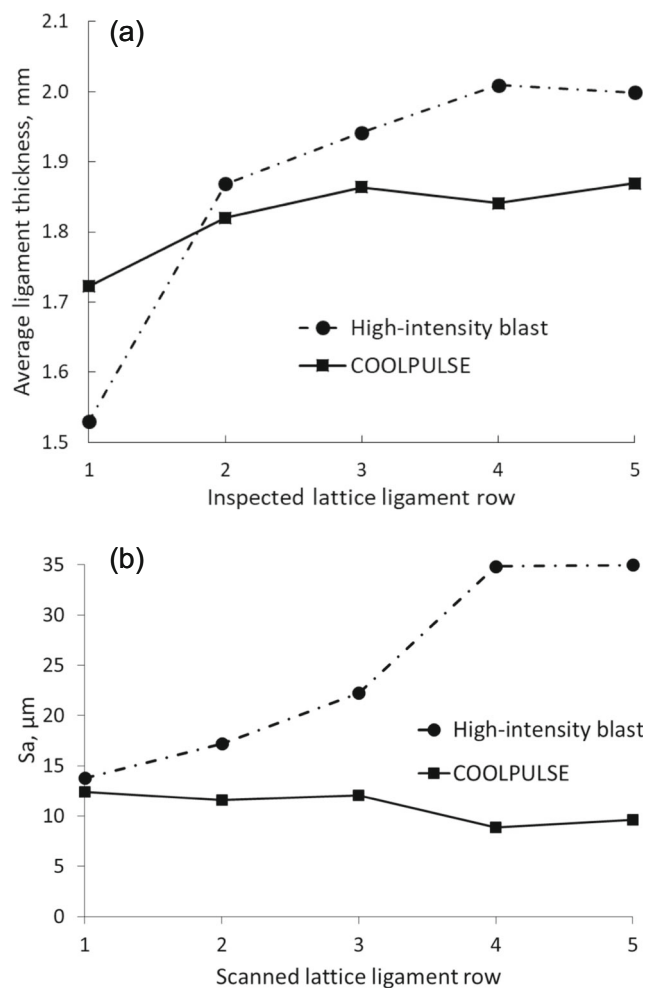

Fig. 19 High-intensity external blasting and COOLPULSE-processed specimens (downskin, side A). **a** Average in-plane horizontal ligament thickness by row (top to bottom). **b** Depth profile of areal average roughness (Sa) of side A lattice interior as measured by WLI. Scan locations were along the third column of vertical ligaments, from location AV13 to AV53. See Fig. 6 for row position diagram

regions of the lattice within the expected range of the cathode prongs. Such processing is expected to result in improvement to critical surface-sensitive properties and enable the type of lightweighting often envisioned by the use of lattices. Though promising, the results of the present study are only a proof of concept, and future work is needed to study process characteristics and limits of the proposed technology.

Numerical modeling was performed using COMSOL Multiphysics finite element software to understand the material removal reported in this study. Predicted current density on the surface of the lattice is shown in 3D in Fig. 20a, where the inner and outer cathode are outlined in black. Higher reaction rates (red) are present along the faces of the ligaments

directly exposed to the interstitial channels where the cathode tooling prongs are located, indicating that surfaces in closest proximity to the cathode tool are subject to the highest rate of anodic dissolution. Lower reaction rates (yellow and blue) are present in the corners where these ligaments meet and along surfaces not directly exposed to the cathode tool, indicating that surfaces separated by a greater distance experience lower rate of anodic dissolution (Fig. 3b).

A 2D cross section of current density within the electrolyte is shown in Fig. 20b. Current density is highest around the inner cathode prong, having converged from the lattice anode's larger available surface area. The location at the surface of the workpiece closest to the inner cathode prong has the highest current density. Current density falls off with distance from the inner cathode.

Further mathematical modeling and simulation would benefit the development of this process. In particular, more
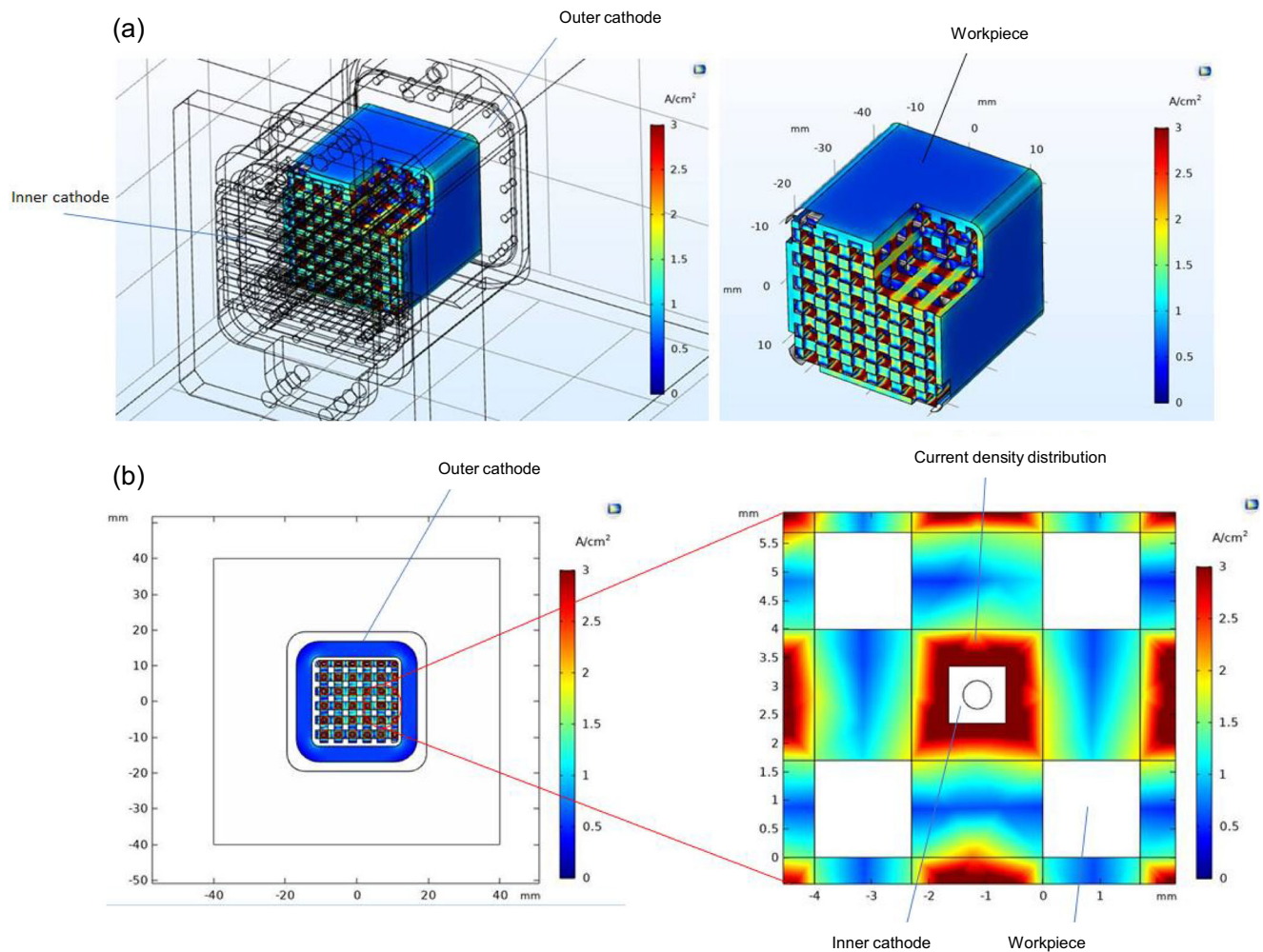
Fig. 20 Simulations of the electrochemical machining process using designed specimens and cathode tooling. **a** 3D and **b** 2D cross section

detailed reaction rate and transport modeling would aid the understanding of reaction rate distribution on the lattice surface. Co-optimization of both cathode tooling shape and lattice form based on these findings has the potential to make overall reaction rates and material removal more uniform.

The present work did not fully explore how deep the surface improvement can extend into the core of a large part. It is possible that the surface improvement could taper off as a function of distance into the cavity, albeit at a much slower rate of decay than the exterior-only jet blasting process (Fig. 19). Potential mitigation strategies are to design remote electrolyte inlets and outlets into a large part to reduce concentration polarization in the electrolyte in regions far from the primary inlet. Future work should scale up from 25 mm lattice cubes.

The specimen used in this work was a simple lattice cube with a straightforward, rectangular lattice that provided line-of-sight for straight internal cathode tool prongs. This allowed for the easy insertion and removal of the cathode. Other lattice topologies [58–60] may not be as simple and therefore may require more complicated tool shape and more complicated insertion strategies, such as curving in a circular arc or corkscrewing. Additionally, overall geometry of complex parts may require more intricate tool shapes or may require insertion of secondary cathode tools in remote regions of the part in order to uniformly finish all lattice. Growing complex and removable tools inside lattice may also be a viable strategy for addressing part complexity. Distortion of tools created by AM is a potential issue, as described previously, and should be addressed in the design stage.

Machining stock is required to be added to the design in order to meet specified final lattice dimensions due to the removal of material during processing. Thus, final lattice design cannot be too dense because sufficient room must be provided for tool insertion as well as for electrolyte circulation. The final design, therefore, should be relatively low density (e.g., ≤40% solid). Stock distribution could be nonuniform as a function of mass and charge transport within a part. Furthermore, opportunity exists for optimization of CP process parameters to achieve maximum material removal rates and good surface integrity.

Finally, future work should validate the effect of the process on properties such as HCF. In addition to reducing roughness and removing material at the surface, the process also resulted in rounding of sharp corners between ligaments. This is beneficial in that stress concentrators that lead to reduction in fatigue life [34, 61] and serve as failure initiation sites [12] are automatically removed, despite being present in both the design and the build.

5 Conclusion

Metal additive manufacturing offers design freedom and the potential to realize hitherto impractical or impossible product designs. One characteristic, and limiting, aspect of metal AM is that of high surface roughness and the presence of defects on surfaces. These features tend to initiate cracks and consequently limit fatigue life, especially in high cycle fatigue, and can serve as a major contributor to pressure loss in applications requiring fluid flow. Machining all over is a common strategy to mitigate the effect of rough surface. It is not possible, however, to address the surface condition of an internal lattice using conventional machining.

In this paper, a strategy for finishing the surfaces of lattices using the commercial electrochemical machining process COOLPUSE was proposed and demonstrated. Inconel 718 lattice coupons and complementary cathode tooling were designed and manufactured. The tooling featured prongs to reach into the core of the lattice coupon in order to establish proximity between cathode and lattice surface (workpiece). The tooling also had ports to allow electrolyte circulation in and around the lattice coupon. Both features had the effect of extending the electrochemically active region from the outside of the part into the core of the lattice.

Inspection of COOLPULSE-processed lattice specimens revealed that a significant amount of material was removed from both internal and external surfaces. White light interferometry showed a change in surface topography and an accompanying reduction in measures of surface roughness on the order of 70% for internal lattice surfaces. Depth profiling of roughness and ligament thickness indicated that the improvement of lattice surface state extended well into the core of the specimen without diminishment. This contrasts with exterior blasting processes where roughness improvement is achieved in the first several unit cells but decreases significantly as a function of depth into the core of the specimen.

The work reported here is preliminary and serves as a proof of concept of a novel cathode tool. It offers the possibility of mitigating the reduction in fatigue life associated with the surfaces of additively manufactured lattices and could also be enabling of parts with optimized and lightweight form factors. Future work should include studying scalability to large parts, higher complexity lattice unit cells and part geometries,

and quantification of the effect on HCF and pressure drop properties.

References

1. Bendsoe MP, Sigmund O (2003) Topology optimization: theory, methods, and applications, 2nd edn. Springer, Berlin
2. Cheng L, Zhang P, Biyikli E, Bai J, Robbins J, To AC (2017) Efficient design optimization of variable-density cellular structures for additive manufacturing: theory and experimental validation. Rapid Prototyp J 23(4):660–667. https://doi.org/10.1108/RPJ-04-2016-0069
3. Challis VJ, Xu X, Zhang LC, Roberts AP, Grotowski JF, Sercombe TB (2014) High specific strength and stiffness structures produced using selective laser melting. Mater Des 63:783–788
4. Shen Y, McKown S, Tsopanos S, Sutcliffe C, Mines R, Cantwell W (2010) The mechanical properties of sandwich structures based on metal lattice architectures. J Sandw Struct Mater 12(2):159–180
5. Murr L, Gaytan S, Medina F, Lopez H, Martinez E, Machado B, Hernandez D, Martinez L, Lopez M, Wicker R (2010) Next-generation biomedical implants using additive manufacturing of complex, cellular and functional mesh arrays. Philos Trans R Soc A Math Phys Eng Sci 368(1917):1999–2032
6. Arabnejad S, Johnston B, Tanzer M, Pasini D (2017) Fully porous 3D printed titanium femoral stem to reduce stress-shielding following total hip arthroplasty. J Orthop Res 35(8):1774–1783
7. Zhu L, Li N, Childs P (2018) Light-weighting in aerospace component and system design. Propul Power Res 7(2):103–119
8. Tang Y, Dong G, Zhou Q, Zhao YF (2017) Lattice structure design and optimization with additive manufacturing constraints. IEEE Trans Autom Sci Eng 15(4):1–17
9. Maheshwaraa U, Seepersad CC (2011) Topology design and freeform fabrication of deployable structures with lattice skins. Rapid Prototyp J 17(1):5–16
10. Brooks H, Brigden K (2016) Design of conformal cooling layers with self-supporting lattices for additively manufactured tooling. Addit Manuf 11:16–22
11. Weeger O, Boddeti N, Yeung S-K, Kaijima S, Dunn M (2019) Digital design and nonlinear simulation for additive manufacturing of soft lattice structures. Addit Manuf 25:39–49
12. Lynch ME, Mordasky M, Cheng L, To AC (2018) Design, testing, and mechanical behavior of additively manufactured casing with optimized lattice structure. Addit Manuf 22:462–471. https://doi.org/10.1016/j.addma.2018.05.021
13. Schaedler TA, Carter WB (2016) Architected cellular materials. Annu Rev Mater Res 46:187–210
14. Wadley HN (2006) Multifunctional periodic cellular metals. Philos Trans R Soc A Math Phys Eng Sci 364(1838):31–68
15. Cabanettes F, Joubert A, Chardon G, Dumas V, Rech J, Grosjean C, Dimkovski Z (2018) Topography of as built surfaces generated in metal additive manufacturing: a multi scale analysis from form to roughness. Precis Eng 52:249–265. https://doi.org/10.1016/j.precisioneng.2018.01.002

16. Stimpson CK, Snyder JC, Thole KA, Mongillo D (2016) Roughness effects on flow and heat transfer for additively manufactured channels. J Turbomach 138(5):051008

17. Fox JC, Moylan SP, Lane BM (2016) Effect of process parameters on the surface roughness of overhanging structures in laser powder bed fusion additive manufacturing. Procedia CIRP 45:131–134. https://doi.org/10.1016/j.procir.2016.02.347

18. Cooper DE, Stanford M, Kibble KA, Gibbons GJ (2012) Additive manufacturing for product improvement at Red Bull Technology. Mater Des 41:226–230

19. Tian Y, Tomus D, Rometsch P, Wu X (2017) Influences of processing parameters on surface roughness of Hastelloy X produced by selective laser melting. Addit Manuf 13:103–112. https://doi.org/10.1016/j.addma.2016.10.010

20. Saltzman DJ, Bichnevicius M, Lynch SP, Simpson T, Reutzel T, Dickman C, Martukanitz R (2017) Experimental comparison of a traditionally built versus additively manufactured aircraft heat exchanger. In: 55th AIAA Aerospace Sciences Meeting. p 0902

21. Ventola L, Robotti F, Dialameh M, Calignano F, Manfredi D, Chiavazzo E, Asinari P (2014) Rough surfaces with enhanced heat transfer for electronics cooling by direct metal laser sintering. Int J Heat Mass Transf 75:58–74

22. Regis M, Marin E, Fedrizzi L, Pressacco M (2015) Additive manufacturing of trabecular titanium orthopedic implants. MRS Bull 40(2):137–144

23. Weißmann V, Drescher P, Seitz H, Hansmann H, Bader R, Seyfarth A, Klinder A, Jonitz-Heincke A (2018) Effects of build orientation on surface morphology and bone cell activity of additively manufactured Ti6Al4V specimens. Materials 11(6):915

24. Kirsch KL, Thole KA (2018) Experimental investigation of numerically optimized wavy microchannels created through additive manufacturing. J Turbomach 140(2):021002

25. Thomas-Seale L, Kirkman-Brown J, Attallah M, Espino D, Shepherd D (2018) The barriers to the progression of additive manufacture: perspectives from UK industry. Int J Prod Econ 198:104–118

26. Yadollahi A, Shamsaei N (2017) Additive manufacturing of fatigue resistant materials: challenges and opportunities. Int J Fatigue 98:14–31

27. Lambert DM (2016) Evaluation of the effect of surface finish on high-cycle fatigue of SLM-IN718, NASA report M16–5137

28. Gockel J, Sheridan L, Koerper B, Whip B (2019) The influence of additive manufacturing processing parameters on surface roughness and fatigue life. Int J Fatigue 124:380–388. https://doi.org/10.1016/j.ijfatigue.2019.03.025

29. Bagehorn S, Wehr J, Maier H (2017) Application of mechanical surface finishing processes for roughness reduction and fatigue improvement of additively manufactured Ti-6Al-4V parts. Int J Fatigue 102:135–142

30. Benedetti M, Torresani E, Leoni M, Fontanari V, Bandini M, Pederzolli C, Potrich C (2017) The effect of post-sintering treatments on the fatigue and biological behavior of Ti-6Al-4V ELI parts made by selective laser melting. J Mech Behav Biomed Mater 71:295–306

31. McCullough K, Fleck N, Ashby M (2000) The stress-life fatigue behaviour of aluminium alloy foams. Fatigue Fract Eng Mater Struct 23(3):199–208

32. Li S, Murr LE, Cheng X, Zhang Z, Hao Y, Yang R, Medina F, Wicker R (2012) Compression fatigue behavior of Ti–6Al–4V mesh arrays fabricated by electron beam melting. Acta Mater 60(3):793–802

33. Hrabe NW, Heinl P, Flinn B, Körner C, Bordia RK (2011) Compression-compression fatigue of selective electron beam melted cellular titanium (Ti-6Al-4V). J Biomed Mater Res B Appl Biomater 99(2):313–320

34. Huynh L, Rotella J, Sangid MD (2016) Fatigue behavior of IN718 microtrusses produced via additive manufacturing. Mater Des 105:278–289

35. Zhao S, Li S, Hou W, Hao Y, Yang R, Misra R (2016) The influence of cell morphology on the compressive fatigue behavior of Ti-6Al-4V meshes fabricated by electron beam melting. J Mech Behav Biomed Mater 59:251–264

36. Jamshidinia M, Wang L, Tong W, Ajlouni R, Kovacevic R (2015) Fatigue properties of a dental implant produced by electron beam melting®(EBM). J Mater Process Technol 226:255–263

37. Dallago M, Winiarski B, Zanini F, Carmignato S, Benedetti M (2019) On the effect of geometrical imperfections and defects on the fatigue strength of cellular lattice structures additively manufactured via selective laser melting. Int J Fatigue 124:348–360

38. Chern AH, Nandwana P, Yuan T, Kirka MM, Dehoff RR, Liaw PK, Duty CE (2019) A review on the fatigue behavior of Ti-6Al-4V fabricated by electron beam melting additive manufacturing. Int J Fatigue 119:173–184

39. Greitemeier D, Palm F, Syassen F, Melz T (2017) Fatigue performance of additive manufactured TiAl6V4 using electron and laser beam melting. Int J Fatigue 94:211–217

40. Denti L, Bassoli E, Gatto A, Santecchia E, Mengucci P (2019) Fatigue life and microstructure of additive manufactured Ti6Al4V after different finishing processes. Mater Sci Eng A 755:1–9

41. Diaz A (2019) Surface texture characterization and optimization of metal additive manufacturing-produced components for aerospace applications. In: Additive Manufacturing for the Aerospace Industry. Elsevier, pp 341–374

42. Boschetto A, Bottini L, Veniali F (2018) Surface roughness and radiusing of Ti6Al4V selective laser melting-manufactured parts conditioned by barrel finishing. Int J Adv Manuf Technol 94(5–8):2773–2790

43. Persenot T, Buffiere J-Y, Maire E, Dendievel R, Martin G (2017) Fatigue properties of EBM as-built and chemically etched thin parts. Procedia Struct Integr 7:158–165

44. Rajurkar KP, Sundaram M, Malshe A (2013) Review of electrochemical and electrodischarge machining. Procedia CIRP 6:13–26

45. Ahmadi S, Kumar R, Borisov E, Petrov R, Leeflang S, Li Y, Tümer N, Huizenga R, Ayas C, Zadpoor A (2019) From microstructural design to surface engineering: a tailored approach for improving fatigue life of additively manufactured meta-biomaterials. Acta Biomater 83:153–166

46. Tan KL, Yeo S-H, Ong CH (2017) Nontraditional finishing processes for internal surfaces and passages: a review. Proc Inst Mech Eng B J Eng Manuf 231(13):2302–2316

47. Sambharia J, Mali HS (2019) Recent developments in abrasive flow finishing process: a review of current research and future prospects. Proc Inst Mech Eng B J Eng Manuf 233(2):388–399

48. Yang L, Wu Y, Lassell A, Zhou B (2016) Electropolishing of Ti6Al4V parts fabricated by electron beam melting. In: Proceedings of the International Solid Freeform Fabrication (SFF) Symposium, Austin, TX

49. Pyka G, Burakowski A, Kerckhofs G, Moesen M, Van Bael S, Schrooten J, Wevers M (2012) Surface modification of Ti6Al4V open porous structures produced by additive manufacturing. Adv Eng Mater 14(6):363–370

50. Łyczkowska E, Szymczyk P, Dybała B, Chlebus E (2014) Chemical polishing of scaffolds made of Ti–6Al–7Nb alloy by additive manufacturing. Arch Civil Mech Eng 14(4):586–594

51. Lhuissier P, De Formanoir C, Martin G, Dendievel R, Godet S (2016) Geometrical control of lattice structures produced by EBM through chemical etching: investigations at the scale of individual struts. Mater Des 110:485–493

52. de Formanoir C, Suard M, Dendievel R, Martin G, Godet S (2016) Improving the mechanical efficiency of electron beam melted titanium lattice structures by chemical etching. Addit Manuf 11:71–76

53. Van Hooreweder B, Apers Y, Lietaert K, Kruth J-P (2017) Improving the fatigue performance of porous metallic biomaterials produced by selective laser melting. Acta Biomater 47:193–202

54. Cutolo A, Neirinck B, Lietaert K, de Formanoir C, Van Hooreweder B (2018) Influence of layer thickness and post-process treatments on the fatigue properties of CoCr scaffolds produced by laser powder bed fusion. Addit Manuf 23:498–504

55. Extrude Hone. https://extrudehone.com/coolpulse-technology-extrude-hone. Accessed 25 Jan 2021

56. Matt P, Wosniak FA (2019) Method and apparatus for electrolytic polishing and method for fabricating a cathode. Germany Patent DE102016114969A1, 2019

57. ISO 25178-2 (2012) Geometrical product specifications (GPS) — Surface texture: Areal — Part 2: Terms, definitions and surface texture parameters

58. Hao L, Raymont D, Yan C, Hussein A, Young P (2011) Design and additive manufacturing of cellular lattice structures. In: The International Conference on Advanced Research in Virtual and Rapid Prototyping (VRAP). Taylor & Francis Group, Leiria. pp 249–254

59. McMillan M, Jurg M, Leary M, Brandt M (2015) Programmatic lattice generation for additive manufacture. Procedia Technol 20: 178–184

60. Chang P (2011) An improved size, matching, and scaling synthesis method for the design of meso-scale truss structures. Thesis, Georgia Institute of Technology

61. Abad EMK, Khanoki SA, Pasini D (2013) Fatigue design of lattice materials via computational mechanics: application to lattices with smooth transitions in cell geometry. Int J Fatigue 47:126–136